

# Observation of a stripe phase in a spin-orbit coupled exciton-polariton Bose-Einstein condensate

Marcin Muszyński<sup>1†</sup>, Pavel Kokhanchik<sup>2†</sup>, Darius Urbonas<sup>3</sup>, Piotr Kapuściński<sup>1</sup>, Przemysław Oliwa<sup>1</sup>, Rafał Mirek<sup>3</sup>, Ioannis Georgakilas<sup>3</sup>, Thilo Stöferle<sup>3</sup>, Rainer F. Mahrt<sup>3</sup>, Michael Forster<sup>4</sup>, Ulrich Scherf<sup>4</sup>, Dmitriy Dovzhenko<sup>5</sup>, Rafał Mazur<sup>6</sup>, Przemysław Morawiak<sup>6</sup>, Wiktor Piecek<sup>6</sup>, Przemysław Kula<sup>7</sup>, Barbara Piętka<sup>1</sup>, Dmitry Solnyshkov<sup>2,8</sup>, Guillaume Malpuech<sup>2\*</sup>, Jacek Szczytko<sup>1\*</sup>

<sup>1</sup>*Institute of Experimental Physics, Faculty of Physics, University of Warsaw, Poland*

<sup>2</sup>*Université Clermont Auvergne, Clermont Auvergne INP, CNRS, Institut Pascal, F-63000 Clermont-Ferrand, France*

<sup>3</sup>*IBM Research Europe – Zurich, Säumerstrasse 4, 8803 Rüschlikon, Switzerland*

<sup>4</sup>*Macromolecular Chemistry Group and Wuppertal Center for Smart Materials & Systems (CM@S), Bergische Universität Wuppertal, Gauss Strasse 20, 42119 Wuppertal, Germany*

<sup>5</sup>*School of Physics and Astronomy, University of Southampton, Southampton SO17 1BJ, United Kingdom*

<sup>6</sup>*Institute of Applied Physics, Military University of Technology, Warsaw, Poland*

<sup>7</sup>*Institute of Chemistry, Military University of Technology, Warsaw, Poland*

<sup>8</sup>*Institut Universitaire de France (IUF), 75231 Paris, France*

\* marks corresponding authors, E-mails: guillaume.malpuech@uca.fr, jacek.szczytko@fuw.edu.pl

†: these authors contributed equally to this work.

## Abstract

In Bose-Einstein condensates, spin-orbit coupling <sup>1</sup> produces supersolidity <sup>2,3</sup>. It is a peculiar state of matter, which, in addition to the superfluid behaviour of weakly interacting Bose condensates, shows a periodic modulation of its density typical for crystals <sup>4</sup> and called stripe phase <sup>1-3</sup>. Here, we report the fabrication of a new type of samples allowing to achieve room-temperature supersolidity for a quantum fluid of light <sup>5</sup>. The structure is an optical microcavity filled with a nematic liquid crystal (LC) sandwiched between two layers of the organic polymer MeLPPP. We demonstrate the formation of cavity exciton-polaritons in the presence of Rashba-Dresselhaus spin-orbit coupling (RDSOC) <sup>6</sup>, which is tuned by external voltage controlling the LC birefringence. In the RDSOC regime, we demonstrate exciton-polariton condensation <sup>7</sup> in the two distinct degenerate minima of the dispersion. The condensate real space distribution shows both polarization and density stripes, which stem from the interference between phase-coherent condensate components characterized by different wavevectors and polarizations. The possibilities offered by this platform to tune the particle dispersion and to perform full state tomography <sup>8</sup>, including time-resolved <sup>9</sup>, open wide perspectives for detailed future studies of the static and dynamical behaviour of supersolids and of quantum fluids in presence of SOC and topologically non-trivial bands.

Optical microcavities recently appeared as a paradigmatic system to engineer photonic modes demonstrating topological singularities and topological transitions <sup>6,8,10-20</sup>. Topological singularities are parabolic band touchings characterized by a winding number two <sup>10,11</sup>, Dirac point pairs which can be of same sign <sup>8,12</sup> or of opposite signs <sup>14,16,19</sup>, split Dirac points (massive Dirac Hamil-

tonian)<sup>8,21</sup>, and in non-Hermitian cases exceptional points<sup>13,19,22</sup>. The key ingredient behind this richness is the spin-orbit coupling (SOC) of light, but also the full tomographic access to the particle wavefunctions in this platform<sup>8</sup>. The most prominent SOC, which was described quasi simultaneously in planar cavities<sup>10</sup> and in other systems<sup>23</sup>, is related to the transverse (TE-TM) nature of light modes. Another one is an emergent Rashba-Dresselhaus SOC (RDSOC), which was more recently discovered<sup>6</sup> and which occurs when Fabry-Pérot modes of different parities and different polarizations are brought in resonance by a large linear birefringence. In that perspective, the realization of cavities filled with nematic liquid crystals (LCs)<sup>6,15,24,25</sup> represented a breakthrough, since it allows to tune linear birefringence and to control RDSOC on demand. A key aspect of RDSOC with respect to TE-TM SOC is that it scales linearly with the wavevector, and therefore, the resulting dispersion shows two degenerate minima at  $\pm k_0$ . As a result, an equilibrium condensate can show a persistent spin helix (polarization stripes)<sup>26-28</sup>, but also density stripes<sup>1</sup>. By combining superfluid properties with solid-like stripes, an implementation of a supersolid was observed in atomic BEC<sup>2,3</sup>. The existence of the supersolid phase is expected in a broad range of quantum fluids, including the neutron stars<sup>29</sup>.

When strongly mixed with excitonic resonances, photonic modes (polaritons) acquire new properties. One is the time-reversal symmetry breaking by the exciton Zeeman splitting which, combined with SOC, is the ground for realizing photonic Chern insulators at optical frequencies<sup>30,31</sup>. Another crucial new property is the polariton-polariton interaction which was initially demonstrated through its role in non-linear optics<sup>32</sup> and then brought up the concept of quantum fluids of light<sup>5</sup>. A polariton quantum fluid can be generated by a spontaneous BEC process<sup>7</sup>,

which can occur close to thermal equilibrium <sup>33</sup>. It can also be created by resonant excitation allowing to generate metastable superfluid flows <sup>34</sup> up to room temperature in organic-based cavities <sup>35</sup>. The cavity exciton-polariton platform is therefore ideal for the study of quantum fluids behaviour in presence of SOC and in topologically non-trivial bands.

The combination of strong exciton-photon coupling with mode tunability including the RD-SOC regime has so far been achieved using lead halide perovskite as an active material <sup>20,24,25,36</sup>. These materials suffer from limited stability against photo-excitation and also naturally degrade with time due to moisture effect <sup>37</sup>. As an alternative, organic polymer MeLPPP <sup>38</sup> appears quite suitable. It has demonstrated exciton-polariton condensation at room temperature <sup>39-41</sup> with good photostability when encapsulated with thin oxide layers <sup>42</sup>.

In this work, we report the fabrication of an original microcavity with embedded nematic LC and MeLPPP. We prove the formation of strongly coupled exciton-photon modes with a Rabi splitting of 93 meV. We demonstrate the tunability of these modes in a wide spectral range by an external electric field controlling the linear birefringence, allowing to reach the RDSOC regime. We show the polariton condensation with a controlled polarization of the emission. In the RDSOC regime, we observe both spin stripes (spin helix) and density stripes, whose contrast is controlled by mode detuning and which are considered a fingerprint of supersolidity <sup>3</sup>. We also show a clear signature of interaction between the condensate and the exciton reservoir through the presence of a non-equilibrium condensate component populating the negative mass states of the dispersion. These observations are in good agreement with simulations based on the hybrid Boltzmann-Gross-



Pitaevskii equation for a spinor condensate in the presence of RDSOC.

A scheme of the fabricated sample is shown in Fig. 1(a) (details given in Methods). It consists of  $\text{SiO}_2/\text{Ta}_2\text{O}_5$  distributed Bragg reflectors (DBRs), which form a Fabry-Pérot resonator hosting a series of longitudinal modes labeled by their integer order. A nematic LC is embedded within the cavity. By applying a voltage to ITO electrodes, LC molecules rotate in the  $yz$  plane defined by orienting layers, thus providing a tunable birefringence. The LC refractive indices along the ordinary and extraordinary axes are  $n_o \approx 1.57$  and  $n_e \approx 1.98$ , respectively. Modes polarized along  $y$  under normal incidence (H) are tunable by LC rotation, while modes polarized along  $x$  (V) are not affected by voltage. However, both can be tuned by changing the position on the sample thanks to the cavity wedge. Two 35 nm-thick layers of methyl-substituted ladder-type poly(p-phenylene) (MeLPPP;  $M_n = 31,500$ ,  $M_w = 79,000$ ) showing excitonic resonances surround the LC layer. Details on the optical response of MeLPPP excitons are provided in Methods (extended data figure 3) and in Refs. <sup>39,40</sup>.

The sample is analyzed by angle-resolved photoluminescence (PL) (details in Methods, extended data figure 1). Fig. 1(c-e) shows several of these spectra detected in H-polarization. The modes 15H and 14V enter in resonance at 3 V (Fig. 1(c)) giving rise to the typical "Rashba" spectrum (RDSOC regime). At all voltages, the dispersion and polarization at small  $k_x$  are described (black lines in Fig. 1(c)) by a 2x2 Hamiltonian including the RDSOC coupling between H and V <sup>6</sup> which reads:

$$H_{RDSOC} = \frac{\hbar^2 k^2}{2M} I + (\Delta + \gamma k^2) \sigma_x + 2\alpha k_x \sigma_z \quad (1)$$

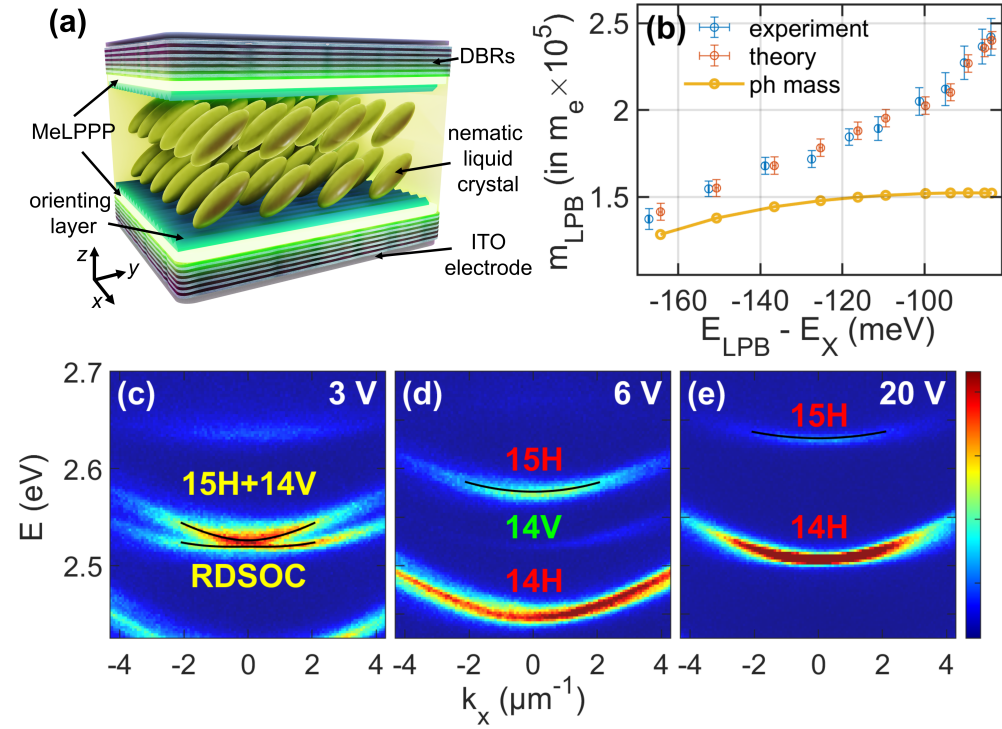


Figure 1: **Demonstration of strong coupling regime.** (a) Microcavity scheme: thick LC layer sandwiched between two organic polymer layers (MeLPPP), two DBRs, and two ITO electrodes; (b) LPB mass as a function of LPB detuning: extracted from the experiment (blue dots) and numerical simulation (red dots); numerical model uses the mode photonic mass at each voltage (yellow dots); (c,d,e) experimentally measured angle-resolved PL for different values of voltage, showing tunability of the H polarized modes and (c) reach of the RDSOC regime; red, green and yellow text labels the number and polarization of the mode(s); black solid lines show the fitting (c) by Hamiltonian (1) and (d,e) by parabola; the excitonic resonance is centered at  $E_X = 2.715$  eV.

with  $I$  the identity matrix,  $\sigma_{x,z}$  are Pauli matrices,  $\Delta = E_V - E_H$  is the H-V detuning, often called Raman coupling in atomic systems,  $M = 2m_V m_H / (m_H + m_V)$ ,  $\gamma = \hbar^2 / 2m$ ,  $m = 2m_V m_H / (m_H - m_V)$ ,  $\alpha$  the RDSOC coupling constant.

With increasing voltage (Fig. 1(c-e)), the mode 15H quits the strong RDSOC regime and approaches the exciton resonance energy  $E_X = 2.715$  eV from below. The mass of the mode is visibly increasing, indicating the strong light-matter coupling. The mass of this lower polariton branch (LPB) is extracted by fitting the PL with a parabola shown in black solid line. The mass dependence versus LPB detuning  $E_{LPB} - E_X$  (controlled by voltage) is shown in Fig. 1(b). In order to fit this experimental dependence and extract the value of Rabi splitting  $\Omega$  we write the Tavis-Cummings model taking into account the inhomogeneous broadening for excitons in MeLPPP (see Methods). The model includes a single photonic mode, defined by its mass and energy obtained from the Berreman method simulation, and  $N$  excitons, having Gaussian distribution of their energies and each coupled to a photonic mode with the coupling strength  $\hbar g = \Omega / \sqrt{N}$ . Therefore, for each voltage, our theoretical model provides both the LPB energy and mass which we plot in Fig. 1(b). The extracted Rabi splitting is  $\Omega = 93$  meV. The constructed model is equivalent to the coupled oscillator model with two oscillators coupled by  $\Omega$  for big exciton-photon detunings, while the behavior of the two models diverges when the detuning is reduced. We also extract the LPB exciton fraction of  $\approx 5.5\%$  at RDSOC regime (Fig. 1(c)). These results confirm the achievement of exciton-photon strong coupling with RDSOC.

We now consider strong optical pumping, demonstrating room temperature exciton-polariton

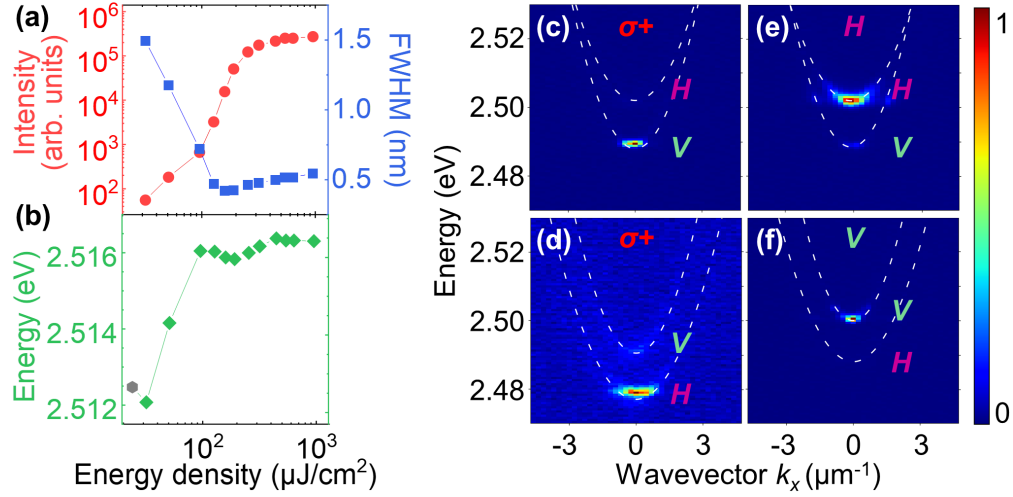


Figure 2: **Controllable polariton condensation.** (a) Emission intensity (red dots), linewidth (blue squares), and (b) mode energy (green diamonds) as a function of the excitation density. An extra point from reflectivity (gray hexagon) added for comparison. (c-f) Normalized angle-resolved PL collected above the condensation threshold. Polarization of the modes is marked with H and V, polarization of the pump is marked in the top middle. Upper panels  $\Delta < 0$ , bottom panels  $\Delta > 0$ . For  $\sigma+$  pumping, condensation occurs in V mode for negative  $\Delta$  (c) and H mode for positive detuning  $\Delta$  (d). (e,f) Linearly-polarized pump. Condensation occurs in the mode having the same polarization as the pump.

condensation. We used pulsed non-resonant excitation (see details in Methods), and our observations are the result of averaging over 500-2500 pulses. First, we consider well-separated linearly polarized modes. Fig. 2(a,b) shows, for one set of parameters, the PL emission intensity, linewidth, and energy of the V-polarized polariton mode versus V-polarized pumping density. The exponential increase in emission intensity, the narrowing of the linewidth, and the weak blueshift provide evidence of polariton condensation. The threshold density of  $95 \mu\text{J}/\text{cm}^2$  is comparable to previous reports of MeLPPP polariton condensates<sup>39,40,42</sup>. Polariton condensation is assisted by a vibron resonance and occurs about 200 meV below the excitonic peak in modes with 5% exciton fraction. The blueshift of 4 meV is almost 3 times lower than the 11 meV difference between the LPB and bare photon energies (exciton-photon detuning of  $-192$  meV). This demonstrates that the strong coupling regime holds in the condensate regime. Also, spatial coherence measurements are shown on extended data figure 2.

Our cavity provides an independent control over the energy of the polarized polaritonic modes: for V and H through changing the position on the sample (cavity wedge) and for H with respect to V ( $\Delta$ ) through the applied voltage. We utilize these features to select the polariton condensate polarization. When the non-resonant pump is circularly polarized, the mode at which the condensation occurs is the one closest to the observed maximum polariton gain. By tuning voltage, the condensation switches from V-polarized to H-polarized mode (Fig. 2(c,d)). Under linearly-polarized pumping, the excitonic reservoir retains a part of this polarization<sup>39</sup> due to selective excitation of chromophores and slow depolarization through energy transfer. This favors the condensation in the state with the same linear polarization (Fig. 2(e,f)).

In the remaining part we study the condensation in the RDSOC regime. Fig. 3(a) shows the k-space emission above the condensation threshold at 0 V, when linearly polarized modes are well separated (as in Fig. 2). The real-space emission is shown in Fig. 3(d). It is affected by disorder, showing bright spots on an homogeneous background of 25  $\mu\text{m}$ , comparable with the pump spot size. The emission is fully linearly polarized (Fig. 3(g)), with no circular polarization (Fig. 3(j)). The Fourier transform of the real space density (Fig. 3(m)) demonstrates the absence of any spatial periodicity.

By changing voltage on the same sample point, two modes of opposite parity come into resonance, turning on RDSOC (Fig. 3(b)). The bands show two minima at  $\pm k_0 \approx 1 \mu\text{m}^{-1}$ . The dispersion is well described by the effective Hamiltonian (1) with  $\Delta = -1.3 \text{ meV}$  and  $\alpha = 2.7 \text{ meV}\cdot\mu\text{m}$ . This Hamiltonian yields  $k_0$  as:

$$k_0 \approx \frac{2M}{\hbar^2} \sqrt{\alpha^2 - \frac{\hbar^2 \Delta^2}{4\alpha^2}}. \quad (2)$$

The eigenstates at two minima are elliptically-polarized with opposite circular polarization degree and same linear polarization degree (see Methods). The experimentally-measured linear polarization degree is 16%. Its analytical value is:

$$S_1 = \frac{\Delta + \gamma k_0^2}{\sqrt{4\alpha^2 k_0^2 + (\Delta + \gamma k_0^2)^2}}, \quad (3)$$

yielding 0.23. If one considers an equilibrium BEC forming in two degenerate dispersion minima, the interference between these components generates polarization stripes (spin helix), whose contrast is given by the circular polarization degree ( $\approx 80\%$ ), and density stripes with a contrast given by the linear polarization degree ( $\approx 16 - 18\%$ ), see Methods. The stripes period is theo-

retically given by  $\pi/k_0$ . Contrary to the atomic condensate case <sup>43</sup>, it is not related to a spatial period imposed by an external laser, but results from the spontaneously-formed coherence of two condensates degenerate in energy but with different momenta.

Indeed, the real space emission (Fig. 3(e)), besides being affected as at 0 V by disorder, shows vertical stripes parallel to the  $y$ -axis. The regularity of this modulation is demonstrated in Fig. 3(m) where the Fourier transform of the real space emission (solid line) demonstrates a peak at  $k_x = 2k_0 = 3.1 \mu\text{m}^{-1}$  in reasonable agreement with the one expected from direct k-space measurements. The ratio between the intensity of the diffraction peak and the one at  $k_x = 0$  gives an estimate of the stripes contrast (2.2%). The polarization stripes period (Fig. 3(h)) is similar to the one of the density stripes, whereas their contrast is 40%. This value sets a minimal mutual coherence degree for the two condensates, in spite of the multishot character of the experiment, which could possibly wash out a 100 % phase coherence giving the same result as if the two states were non-coherent. The observation of stripes in that regime therefore demonstrates the presence of a phase locking mechanism between the components at  $\pm k_0$ . As verified in the numerical simulations below, the phase locking appears due to the inhomogeneous spatial gain profile, which is expected to follow the Gaussian shape of the non-resonant pump laser. A stripe profile with a maximum coinciding with maximal gain is favoured with respect to other profiles making stripes observable. We stress that this pump-induced gain profile does not impose the observed spatial period, but just acts as a kind of seed fixing the preferential positions of the stripes.

Going back to the k-space (Fig. 3(b)), we see that not just the dispersion minima are occupied,

but a strong emission also comes from the negative mass state of the lower branch at  $k = 0$ . This feature is well known for polaritons created by a localized non-resonant pump which induces a repulsive potential. Positive-mass polaritons flow away<sup>44</sup>, whereas negative-mass polaritons are effectively attracted by pump<sup>45,46</sup> and show a higher gain, as we observe.

We simulate polariton condensation under non-resonant pumping using the hybrid Boltzmann-Gross-Pitaevskii equation with lifetime, energy relaxation, and saturated gain<sup>47</sup>:

$$i\hbar \frac{\partial \psi_{\pm}}{\partial t} = (1 - i\Lambda) \hat{T}_{\pm} \psi_{\pm} + i\gamma(|\psi|^2) \psi_{\pm} + U \psi_{\pm} + \Delta \psi_{\mp} + \chi. \quad (4)$$

Here,  $\hat{T}_{\pm}$  is the kinetic energy operator containing terms accounting for several effects: the dispersion relation of polaritons with mass  $m$ , the gauge potential contribution of the RDSOC  $-2i\alpha \cdot \partial \psi_{\pm} / \partial x$ , and the energy relaxation mechanisms<sup>48</sup> via  $\Lambda$ , with zero energy level set at the bottom of the dispersion.  $U = U_0 \exp(-r^2/2\sigma^2)$  is the repulsive potential of the reservoir.  $\gamma(|\psi|^2)$  is the term combining decay and saturated gain,  $\chi$  is the noise describing the spontaneous scattering from the excitonic reservoir. The saturated gain is given by  $\gamma(|\psi|^2) = \gamma_0(n_R) \exp(-n_{tot}/n_s)$  with  $n_{tot} = \int |\psi|^2 dx dy$  the total particle density,  $n_s$  the saturation density, and  $n_R$  the exciton reservoir density. We solve Eq. (4) numerically using the parameters of the polariton dispersion determined from the experimental results presented in Fig. 3. Other parameters were taken as  $\Lambda = 0.02$ ,  $U_0 = 0.1$  meV,  $\sigma = 18$   $\mu\text{m}$ . In k-space (Fig. 3(c)) we observe several condensation energies due to the non-equilibrium nature of polariton condensation<sup>33</sup>. We observe a weak population at the bottom of the upper branch, and a strong population in the negative mass state



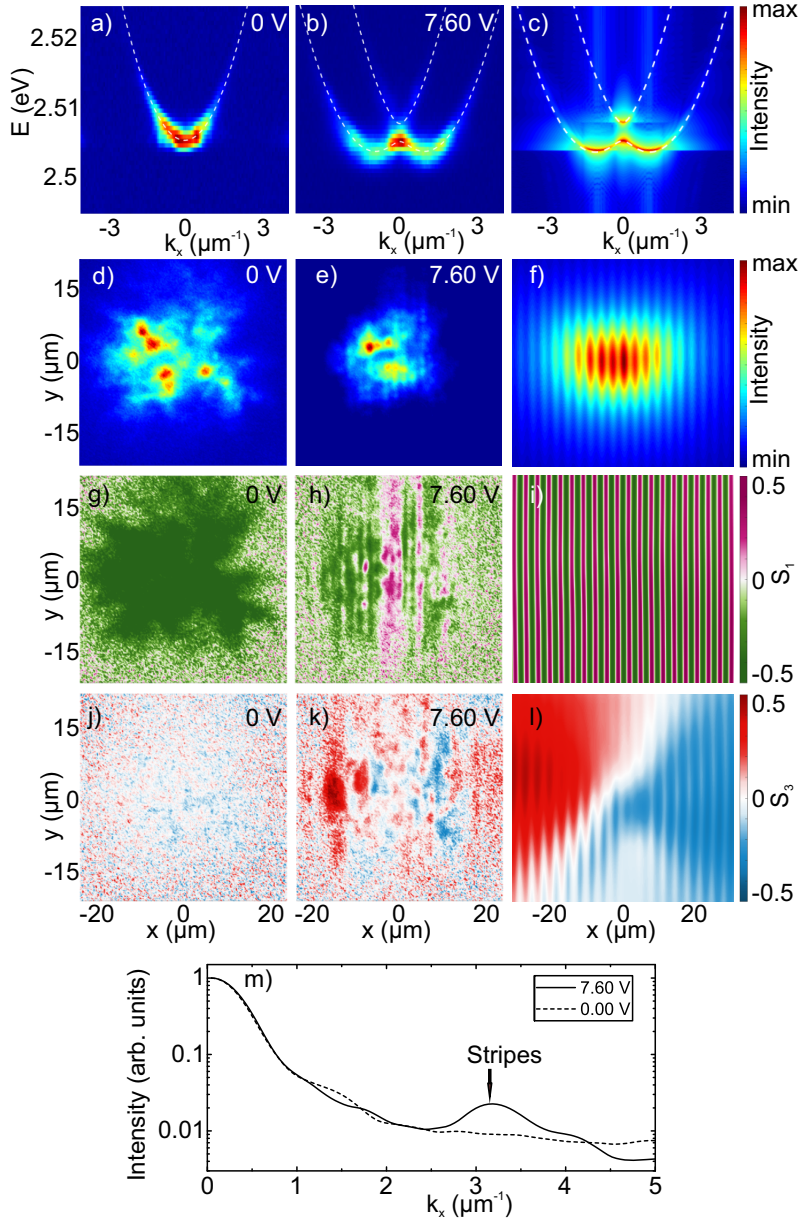


Figure 3: **Stripe phase in a polariton condensate.** Photoluminescence measured at 0 V (first column), 7.6 V in the presence of RDSOC (second column) and calculated (third column). The first row (a-c) shows the  $k_x$ -dependent total emission with the double minima dispersion in (b,c). The second row (d-f) shows the real space total emission with stripes absent in (d) and present in (e,f). The third (g-i) and fourth (j-l) rows show the real space distribution of the linear  $S_1$  and circular  $S_3$  polarization degree, respectively. (m) Fourier transform of the experimental intensity from (d,e) with a marked stripes diffraction peak.

near  $k_x = 0$ , as discussed above. The most populated component is at the two minima of the lower branch. It is possible to favor one of these components by tuning parameters, in particular the relaxation parameter  $\Lambda$ . The real space emission Fig. 3(f) shows the expected stripes with a maximum coinciding with the maximum of the Gaussian gain profile. The circular polarization degree, besides the stripes, shows a spatial separation as in the experiment (Figs. 3(k,l)). This spatial separation is present due to the circular polarization degree asymmetry between the dispersion minima at  $\pm k_0$  for non-zero  $\Delta$ . The spatial profiles of both density and polarization slightly vary from one simulation to another. This is due to the random formation of vortices taking place during the condensation process via the Kibble-Zurek mechanism<sup>49,50</sup>. This type of effect could be accessed by single shot experiments, which are possible for these types of samples as shown in the extended data figure 2, where we present single-shot coherence measurements. It could also allow to access the relative phase fluctuations associated with stripes displacement, which despite the gain phase-locking mechanism, are certainly still present. On the other hand, these experiments are really challenging because of the reduced signal to noise ratio and we let the detailed study of these effects, and in general the study of the dynamical behaviour of the supersolid phase, for future works.

A specificity of this platform with respect to atomic condensates is the mass difference  $\gamma$  between two linearly polarized modes coupled by the RDSOC. It ensures the presence of stripes even at zero detuning  $\Delta$  with a contrast  $M/2m$ . However, stripes disappear at a particular non-zero value of detuning  $\Delta = -\gamma k_0^2$ .

In summary, We demonstrated strong light-matter coupling in an optical microcavity with embedded LC and photostable MeLPPP polymer. We observed polariton condensation first in the regime where photonic bands of the cavity are well separated and we demonstrated the tunability of the condensate polarization by either the external voltage or the pump polarization. In the RDSOC regime, non-equilibrium condensate forms simultaneously in the negative mass state of the dispersion, being a signature of the repulsive interaction with the excitonic reservoir, and in two degenerate minima. The real space distributions of polarization and intensity show stripes. In equilibrium BEC, a stripe phase is considered as a signature of supersolidity<sup>2,3</sup>, combining the periodic spatial modulation of solids and superfluidity, where a Hermitian defect can move without perturbing stripes. Our work opens new perspectives for quantum fluids of light physics in presence of SOC and beyond, in topologically non-trivial systems.

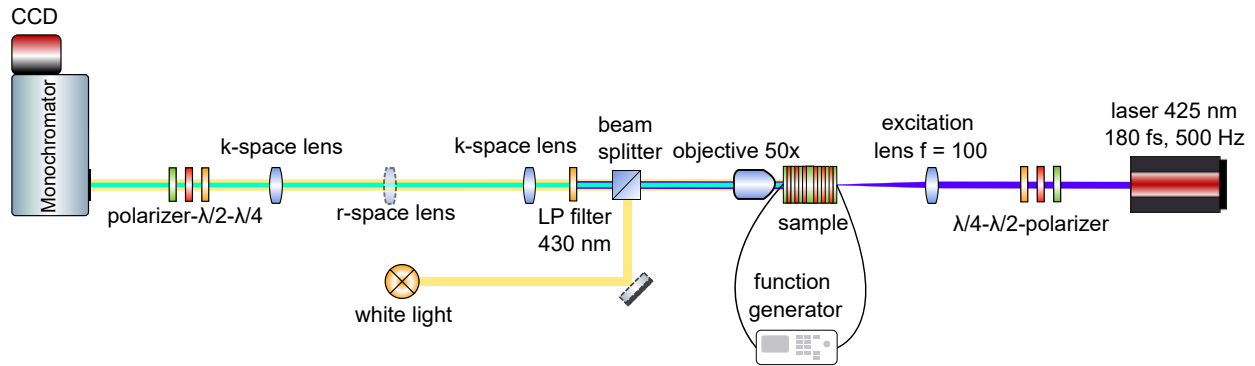
## Methods

**Sample preparation.** The cavity consists of two distributed Bragg reflectors (DBRs) composed of 15 and 13  $\text{SiO}_2/\text{Ta}_2\text{O}_5$  layers, with a central wavelength at 490 nm. The DBRs were deposited on 30 nm ITO electrode layers on quartz substrates with a flatness of  $\lambda/20$ (@633 nm). Both DBRs were spin-coated with 35 nm MeLPPP layers covered with protective  $\text{Al}_2\text{O}_3$  layers of 20 nm thickness. Antiparallel orienting layers (SE-130, Nissan Chem., Japan) were deposited on both substrates using the spin-coating method. The wedge cavity was achieved using glass spacers with sizes of 1.5 – 2  $\mu\text{m}$  placed between the substrates. The cavity was filled with a liquid crystal mixture, LC2091\* (refractive indices  $n_o \approx 1.57$  and  $n_e \approx 1.98$ , for the sodium line 589 nm), in the

nematic phase by capillary action.

**Experimental details.** Extended Data Figure 1 presents the optical experimental setup. The optical measurements are performed at room temperature. The reflectivity measurements employ the microscope objective with 50x magnification, numerical aperture  $NA = 0.65$  for both the excitation and the collection of light. The spot has a diameter of around  $10 \mu\text{m}$  on the sample. In photoluminescence measurements, an additional lens  $f = 100 \text{ mm}$  is used to focus the excitation laser onto the  $20 \mu\text{m}$  spot on the surface of the sample. The 181 fs pulsed laser of 425 nm wavelength and repetition rate of 500 Hz is used for non-resonant excitation. Depending on the selected lenses ( $k$ -space or  $r$ -space) and the light source, the setup allows measuring the reciprocal space, as well as the real space at the same position on the sample. Two sets of a quarter-wave plate, a half-wave plate, and a linear polarizer are used to control the polarization of the excitation and collected signal. To tune the dispersion relation of the cavity modes, the LC microcavity is addressed by an AC waveform generator with a 1010 Hz square signal and varying amplitude of 0 – 20 V. Paths of white light are indicated by yellow lines, the laser light path is marked with a blue line, and the signal from the sample is represented by a cyan line.

**Interference measurements.** Extended Data Figure 2 shows the interferogram of a polariton condensate measured at excitation intensity of around  $1.2P_{th}$  with Michelson interferometer. The experiment was not performed simultaneously with the one presented in the main text and was using a slightly different excitation scheme. We non-resonantly excite the condensate using a 6 ns pulsed laser at a 425 nm wavelength in a single-shot regime. Interferometry data were acquired at 0 V, so in the regime of parabolic dispersion (RDSOC off), and with a pump spot of  $20 \mu\text{m}$ . In

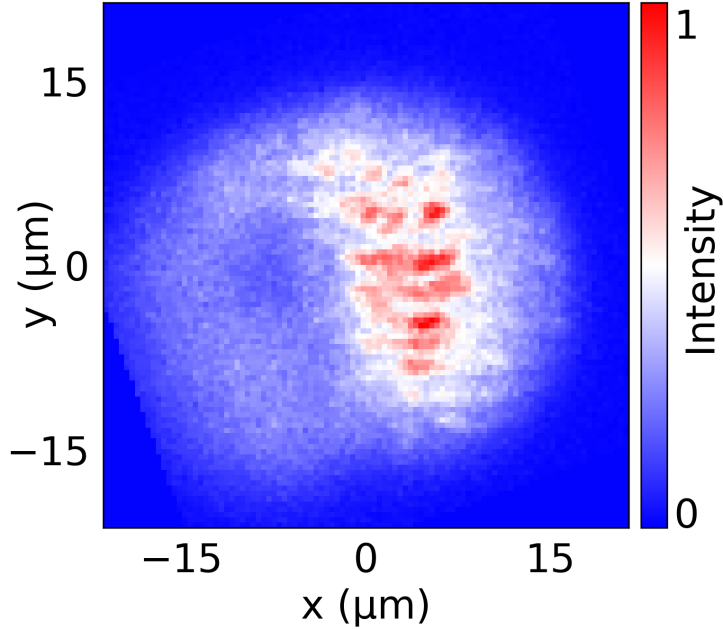


Extended Data Figure 1: Experimental setup scheme.

Extended Data Figure 2 the interference fringes are observed over the whole area of the condensate in the real space, demonstrating a build-up of the long-range spatial coherence, which is a hallmark of the exciton-polariton condensation.

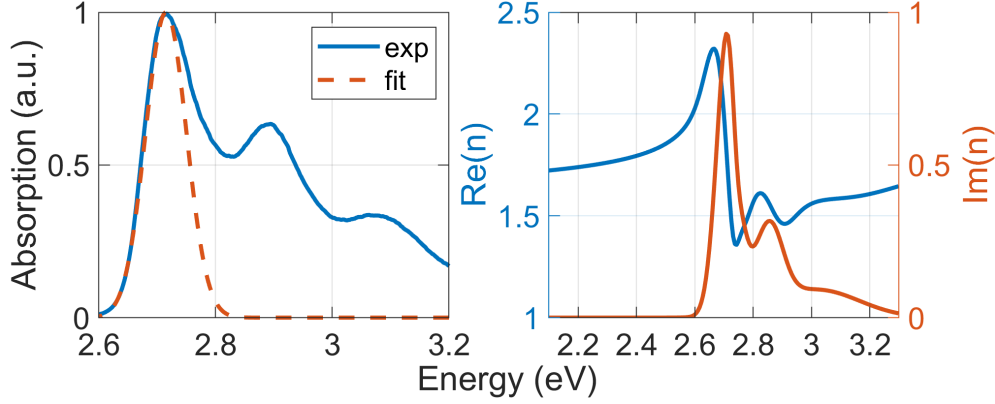
**MeLPPP absorption and complex refractive index** Large inhomogeneous broadening of the excitonic peak plays a significant role in the theoretical treatment of the results. In order to estimate this broadening, we measured the absorption spectrum of a single MeLPPP layer on the DBR and made a fit of the main excitonic peak by Gaussian function  $\exp\{[-(E - E_X)^2/2\sigma^2]\}$ , with  $E_X = 2.715$  eV center of the peak and  $\sigma = 35$  meV standard deviation of exciton energy distribution (Extended Data Figure 3(a)). Since we will be considering only strongly negatively detuned photonic modes, we do not need to take into account higher energy absorption peaks.

Also, we show here the MeLPPP complex refractive index real and imaginary parts (Extended Data Figure 3(b)) which will be used in the next section for the Berreman method simulation of microcavity structure. The background refractive index of MeLPPP extracted from  $\mathbf{Re}(n)$  dependence is  $n_{BG} = 1.7$ .



Extended Data Figure 2: Single-shot interferogram of a polariton condensate at zero delay.

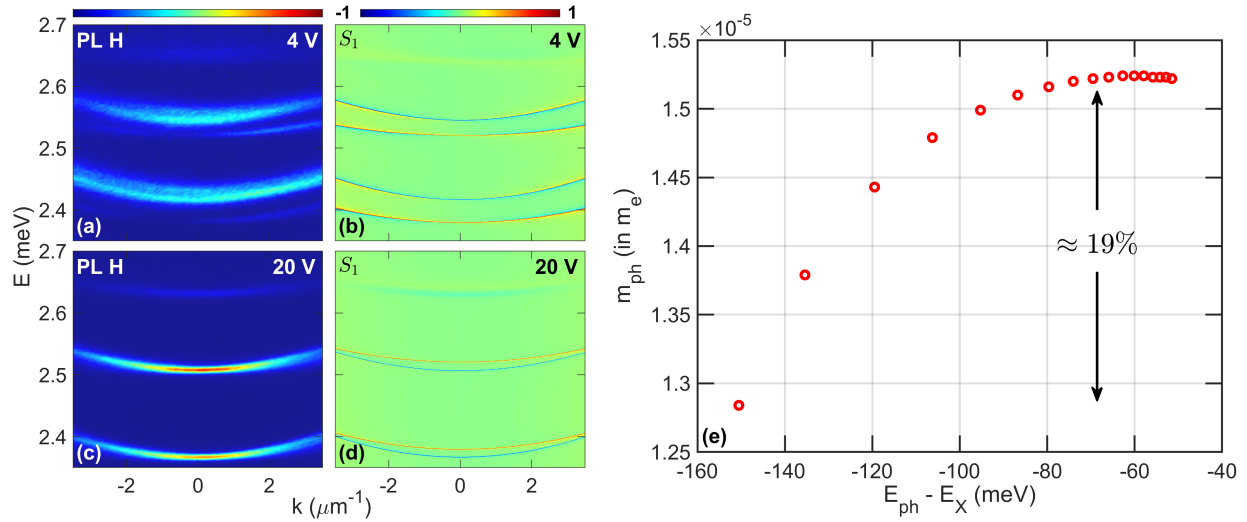
**Photonic mass** Since the mode 15H is tuned over the large range of energies in Fig. 1 (LPB detuning between -188 meV and -84 meV), it is crucial to estimate how the photonic mass of the mode changes in the tuning process. In order to do this, we first reproduce the band structure of the microcavity with the use of the Berreman method<sup>51</sup>. We simulate the structure shown in Fig. 1(a) and tune the length of the LC layer and the angle of LC molecules in order to obtain perfect correspondence between measurement and simulation shown in Extended Data Figure 4. In the experiment, the PL was measured in H polarization, which is why the H mode is well-visible for any voltage applied to the microcavity, while the V mode appears only when it couples to the H mode strongly enough (Extended Data Figure 4(a)). The numerical simulation (Extended Data Figure 4(b,d)) is represented by the first Stokes parameter of the system (linear polarization degree) in order to easily distinguish between H and V modes, appearing as blue and red lines, respectively.



Extended Data Figure 3: **MeLPPP absorption and complex refractive index.** (a) Experimentally measured absorption of a single MeLPPP layer on the DBR (solid blue line); the fit of the main absorption peak by Gaussian function representing inhomogeneous broadening of excitons (dashed red line); (b) real ( $\text{Re}(n)$ , blue line) and imaginary ( $\text{Im}(n)$ , red line) parts of complex refractive index obtained by ellipsometry.

After achieving correspondence between the experiment and numerical simulation, we calculate once again the dispersion for the same structure, except that now the MeLPPP refractive index is constant and equal to background one ( $n = n_{BG}$ ), thus eliminating the exciton from the calculation and making the system purely photonic. Then, we extract the mass and the position of the photonic mode and plot them in Extended Data Figure 4(e). The range of photonic mode detunings  $E_{ph} - E_X$  corresponds to the LPB detunings from Fig. 1(b). One can see that the total change of the photonic mass is approximately 19%. This simulation proves that the much bigger mode effective mass change observed in Fig. 1 can be explained solely by exciton-photon coupling.

**The Tavis-Cummings model** The Tavis-Cummings model describes the system consisting of a single cavity mode coupled to  $N$  two-level systems, excitons in our case. Usually, the model



Extended Data Figure 4: **Photonic mass extraction.** (a,c) Experimentally measured PL in H polarization and (b,d) numerically calculated first Stokes parameter (degree of linear polarization) with the use of the Berreman method for the voltage (a,b) 4 V and (c,d) 20 V applied to the microcavity. (e) Extracted from simulation, the photonic mass as a function of photonic mode detuning. The photonic detunings range corresponds to the LPB detunings range from Fig. 1(b). The total photonic mass change is 19%, proving that the mass change of 76% shown in Fig. 1(b) can be explained only by exciton-photon coupling.



utilizes identical excitons, while in our case non-homogeneous broadening of the excitonic peak plays an important role in quantitative correspondence with experiment. The model reads as:

$$H = \hbar(\omega_{ph} - i\gamma_{ph})a^\dagger a + \sum_{j=1}^N \hbar(\omega_{ex,j} - i\gamma_{ex})\sigma_j^+ \sigma_j^- + \hbar g (a\sigma_j^+ + a^\dagger\sigma_j^-), \quad (5)$$

with  $\hbar\omega_{ph} = \hbar\omega_{ph,0} + \frac{\hbar^2 k_x^2}{2m_{ph}}$  energy of a cavity defined by  $\hbar\omega_{ph,0}$  energy at  $k_x = 0$  and  $m_{ph}$  cavity photon mass,  $\gamma_{ph}$  cavity mode decay,  $\hbar\omega_{ex,j}$  energy of  $j$ -th exciton taken from non-homogeneously broadened Gaussian distribution,  $\gamma_{ex}$  non-radiative decay of a single exciton,  $\hbar g$  exciton-photon coupling strength,  $a^\dagger$  and  $a$  cavity mode creation and annihilation operators, respectively,  $\sigma_j^+ = |e_j\rangle \langle g_j|$  and  $\sigma_j^- = |g_j\rangle \langle e_j|$   $j$ -th two-level system raising and lowering operators, respectively. The total Rabi splitting can be estimated as  $\Omega = \hbar g \sqrt{N}$  for big exciton-photon detunings.

For every voltage, we extracted photonic mode  $\hbar\omega_{ph}$ . Since the characteristic pump spot width ( $w_{pump} \approx 20 \mu\text{m}$ ) is much larger than the estimated transverse cavity photon coherence length ( $l_{coh} \approx 1.5 \mu\text{m}$ ), we consider  $N_{ens} = w_{pump}^2/l_{coh}^2$  different realizations of Hamiltonian (5): each realization differs by excitonic disorder (ensemble of  $\hbar\omega_{ex,j}$ ) and coupled photon. Using extracted photonic data, we diagonalize each realization of the Hamiltonian (5) and for each realization we extract the eigenmode with the highest photonic contribution. Next, we sum up the PL signal originating from these eigenmodes for all wavevectors. After applying this procedure, we obtain a total PL signal similar to the experimental one. We then extract the mass and energy of the numerically obtained LPB, exactly like we do with the experimentally measured PL intensity maps, and plot the final results in Fig. 1(b). As one can see both LPB detuning and mass obtained by numerical simulation correspond well to the experimental data when we choose Rabi splitting of  $\Omega = 93 \text{ meV}$ . The number of excitons used for every realization of Hamiltonian (5) is

$N_X = 200$ . In reality, the number of excitons per each coherent spot  $l_{coh}^2$  should be much bigger, but increasing this number very quickly makes the Hamiltonian diagonalization computationally heavy. That is why we made sure that the simulation results slowly converge when we increase  $N_X$  up to 2000, then we performed all the simulations for  $N_X = 200$  and included the difference as a method error shown by red error bars in Fig. 1(b). The decay values used in simulations are  $\hbar\gamma_{ph} = 3$  meV and  $\hbar\gamma_{ex} = 0.1$  meV <sup>39</sup>.

**Analytical description of the stripes and their contrast** The wave function describing a spinor wavefunction with two contributions corresponding to the eigenstates at two opposite wave vectors  $\pm k_0$  can be written as:

$$|\psi\rangle = \frac{1}{2} \begin{pmatrix} \cos \frac{\theta}{2} \\ \sin \frac{\theta}{2} \end{pmatrix} e^{-ik_0x} + \frac{1}{2} \begin{pmatrix} \cos \frac{\pi-\theta}{2} \\ \sin \frac{\pi-\theta}{2} \end{pmatrix} e^{+ik_0x} \quad (6)$$

where  $\theta$  is the polar angle of the Stokes vector, whereas the azimuthal angle is fixed by the polarization of the coupled modes (H and V).

The corresponding density reads

$$\langle \psi | \psi \rangle = \frac{1}{2} + \frac{1}{2} \cos 2k_0x \sin \theta \quad (7)$$

It exhibits oscillations, whose contrast is  $U = \sin \theta$ . This gives a direct relation between the circular (or linear) polarization degree with the contrast of the stripes observed in total intensity.

## Data availability

The data generated in this study are available in the Open Science Framework (OSF) repository:

[https://osf.io/hvpmn/?view\\_only=dea66a4b12b14ad0ac45451ec4205cc8](https://osf.io/hvpmn/?view_only=dea66a4b12b14ad0ac45451ec4205cc8)

## References

1. Lin, Y.-J., Jiménez-García, K. & Spielman, I. B. Spin-orbit-coupled bose-einstein condensates. *Nature* **471**, 83–86 (2011).
2. Li, J.-R. *et al.* A stripe phase with supersolid properties in spin-orbit-coupled bose-einstein condensates. *Nature* **543**, 91–94 (2017).
3. Geier, K. T., Martone, G. I., Hauke, P., Ketterle, W. & Stringari, S. Dynamics of stripe patterns in supersolid spin-orbit-coupled bose gases. *Physical Review Letters* **130**, 156001 (2023).
4. Leggett, A. J. Can a solid be "superfluid"? *Physical Review Letters* **25**, 1543 (1970).
5. Carusotto, I. & Ciuti, C. Quantum fluids of light. *Reviews of Modern Physics* **85**, 299–366 (2013).
6. Rechcińska, K. *et al.* Engineering spin-orbit synthetic Hamiltonians in liquid-crystal optical cavities. *Science* **366**, 727–730 (2019). URL <https://doi.org/10.1126/science.aay4182>.
7. Kasprzak, J. *et al.* Bose-einstein condensation of exciton polaritons. *Nature* **443**, 409–414 (2006).

8. Gianfrate, A. *et al.* Measurement of the quantum geometric tensor and of the anomalous hall drift. *Nature* **578**, 381–385 (2020).
9. Dominici, L. *et al.* Vortex and half-vortex dynamics in a nonlinear spinor quantum fluid. *Science advances* **1**, e1500807 (2015).
10. Kavokin, A., Malpuech, G. & Glazov, M. Optical spin hall effect. *Phys. Rev. Lett.* **95**, 136601 (2005). URL <https://link.aps.org/doi/10.1103/PhysRevLett.95.136601>.
11. Leyder, C. *et al.* Observation of the optical spin hall effect. *Nature Physics* **3**, 628–631 (2007). URL <https://doi.org/10.1038/nphys676>.
12. Terças, H., Flayac, H., Solnyshkov, D. & Malpuech, G. Non-abelian gauge fields in photonic cavities and photonic superfluids. *Physical Review Letters* **112**, 066402 (2014).
13. Richter, S. *et al.* Voigt exceptional points in an anisotropic zno-based planar microcavity: square-root topology, polarization vortices, and circularity. *Physical Review Letters* **123**, 227401 (2019).
14. Ren, J. *et al.* Nontrivial band geometry in an optically active system. *Nature communications* **12**, 689 (2021).
15. Król, M. *et al.* Observation of second-order meron polarization textures in optical microcavities. *Optica* **8**, 255–261 (2021).

16. Polimeno, L. *et al.* Tuning of the berry curvature in 2d perovskite polaritons. *Nature nanotechnology* **16**, 1349–1354 (2021).
17. Spencer, M. S. *et al.* Spin-orbit–coupled exciton-polariton condensates in lead halide perovskites. *Science Advances* **7**, eabj7667 (2021).
18. Long, T. *et al.* Helical polariton lasing from topological valleys in an organic crystalline microcavity. *Advanced Science* **9**, 2203588 (2022).
19. Król, M. *et al.* Annihilation of exceptional points from different dirac valleys in a 2d photonic system. *Nature Communications* **13**, 5340 (2022).
20. Liang, J. *et al.* Polariton spin hall effect in a rashba–dresselhaus regime at room temperature. *Nature Photonics* **357**, 18 (2024).
21. Hasan, M. Z. & Kane, C. L. Colloquium: Topological insulators. *Rev. Mod. Phys.* **82**, 3045–3067 (2010). URL <https://link.aps.org/doi/10.1103/RevModPhys.82.3045>.
22. Su, R. *et al.* Direct measurement of a non-hermitian topological invariant in a hybrid light-matter system. *Science Advances* **7**, eabj8905 (2021).
23. Bliokh, K. Y., Niv, A., Kleiner, V. & Hasman, E. Geometrodynamics of spinning light. *Nature Photonics* **2**, 748–753 (2008).
24. Łempicka-Mirek, K. *et al.* Electrically tunable berry curvature and strong light-matter coupling in liquid crystal microcavities with 2d perovskite. *Science advances* **8**, eabq7533 (2022).

25. Li, Y. *et al.* Manipulating polariton condensates by rashba-dresselhaus coupling at room temperature. *nature communications* **13**, 3785 (2022).
26. Koralek, J. D. *et al.* Emergence of the persistent spin helix in semiconductor quantum wells. *Nature* **458**, 610–613 (2009).
27. Król, M. *et al.* Realizing optical persistent spin helix and stern-gerlach deflection in an anisotropic liquid crystal microcavity. *Phys. Rev. Lett.* **127**, 190401 (2021). URL <https://link.aps.org/doi/10.1103/PhysRevLett.127.190401>.
28. Muszyński, M. *et al.* Realizing persistent-spin-helix lasing in the regime of rashba-dresselhaus spin-orbit coupling in a dye-filled liquid-crystal optical microcavity. *Physical Review Applied* **17**, 014041 (2022).
29. Poli, E. *et al.* Glitches in rotating supersolids. *Phys. Rev. Lett.* **131**, 223401 (2023). URL <https://link.aps.org/doi/10.1103/PhysRevLett.131.223401>.
30. Nalitov, A., Solnyshkov, D. & Malpuech, G. Polariton z topological insulator. *Physical review letters* **114**, 116401 (2015).
31. Klemmt, S. *et al.* Exciton-polariton topological insulator. *Nature* **562**, 552–556 (2018).
32. Baumberg, J. J. *et al.* Parametric oscillation in a vertical microcavity: A polariton condensate or micro-optical parametric oscillation. *Phys. Rev. B* **62**, R16247–R16250 (2000). URL <https://link.aps.org/doi/10.1103/PhysRevB.62.R16247>.

33. Kasprzak, J., Solnyshkov, D., André, R., Dang, L. S. & Malpuech, G. Formation of an exciton polariton condensate: thermodynamic versus kinetic regimes. *Physical review letters* **101**, 146404 (2008).
34. Amo, A. *et al.* Superfluidity of polaritons in semiconductor microcavities. *Nature Physics* **5**, 805–810 (2009).
35. Lerario, G. *et al.* Room-temperature superfluidity in a polariton condensate. *Nature Physics* **13**, 837–841 (2017).
36. Łempicka Mirek, K. *et al.* Electrical polarization switching of perovskite polariton laser. *Nanophotonics* (2024). URL <https://doi.org/10.1515/nanoph-2023-0829>.
37. Chen, B., Wang, S., Song, Y., Li, C. & Hao, F. A critical review on the moisture stability of halide perovskite films and solar cells. *Chemical Engineering Journal* **430**, 132701 (2022).
38. Scherf, U., Bohnen, A. & Müllen, K. Polyarylenes and poly(arylenevinylene)s, 9 the oxidized states of a (1,4-phenylene) ladder polymer. *Die Makromolekulare Chemie* **193**, 1127–1133 (1992). URL <https://onlinelibrary.wiley.com/doi/abs/10.1002/macp.1992.021930511>.
39. Plumhof, J. D., Stöferle, T., Mai, L., Scherf, U. & Mahrt, R. F. Room-temperature bose–einstein condensation of cavity exciton–polaritons in a polymer. *Nature materials* **13**, 247–252 (2014).
40. Zasedatelev, A. V. *et al.* A room-temperature organic polariton transistor. *Nature Photonics* **13**, 378–383 (2019).

41. Zasedatelev, A. V. *et al.* Single-photon nonlinearity at room temperature. *Nature* **597**, 493–497 (2021).
42. Scafirimuto, F., Urbonas, D., Scherf, U., Mahrt, R. & Stöferle, T. Room-temperature exciton-polariton condensation in a tunable zero-dimensional microcavity. *ACS Photonics* **5**, 85–89 (2018). URL <https://doi.org/10.1021/acsp Photonics.7b00557>.
43. Putra, A., Salces-Cárcoba, F., Yue, Y., Sugawa, S. & Spielman, I. Spatial coherence of spin-orbit-coupled bose gases. *Physical Review Letters* **124**, 053605 (2020).
44. Wertz, E. *et al.* Spontaneous formation and optical manipulation of extended polariton condensates. *Nature physics* **6**, 860–864 (2010).
45. Tanese, D. *et al.* Polariton condensation in solitonic gap states in a one-dimensional periodic potential. *Nature communications* **4**, 1749 (2013).
46. Jacqmin, T. *et al.* Direct observation of dirac cones and a flatband in a honeycomb lattice for polaritons. *Physical review letters* **112**, 116402 (2014).
47. Wertz, E. *et al.* Propagation and amplification dynamics of 1d polariton condensates. *Phys. Rev. Lett.* **109**, 216404 (2012). URL <https://link.aps.org/doi/10.1103/PhysRevLett.109.216404>.
48. Pitaevskii, L. Phenomenological theory of superfluidity near the lambda point. *Sov. Phys. JETP* **8**, 282 (1959).



49. Weiler, C. N. *et al.* Spontaneous vortices in the formation of bose–einstein condensates. *Nature* **455**, 948–951 (2008).
50. Solnyshkov, D. D., Nalitov, A. V. & Malpuech, G. Kibble-zurek mechanism in topologically nontrivial zigzag chains of polariton micropillars. *Physical review letters* **116**, 046402 (2016).
51. Berreman, D. W. Optics in stratified and anisotropic media:  $4 \times 4$ -matrix formulation. *JOSA* **62**, 502–510 (1972).

**Acknowledgements** This work was supported by the National Science Centre grants 2019/35/B/ST3/04147, 2019/33/B/ST5/02658 and 2022/47/B/ST3/02411, 2023/51/B/ST3/03025, and the Ministry of National Defense Republic of Poland Program – Research Grant MUT Project 13-995 and MUT University grant (UGB) for the Laboratory of Crystals Physics and Technology for the year 2021 and the European Union’s Horizon 2020 program, through a FET Open research and innovation action under the grant agreements No. 964770 (TopoLight) and EU H2020 MSCA-ITN project under grant agreement No. 956071 (AppQInfo). Additional support was provided by the ANR Labex GaNext (ANR-11-LABX-0014), the ANR program "Investissements d’Avenir" through the IDEX-ISITE initiative 16-IDEX-0001 (CAP 20-25), the ANR project MoirePlusPlus, and the ANR project "NEWAVE" (ANR-21-CE24-0019).

**Author contributions** J.S., G.M., D.D.S., T.S., R.F.M., W.P., B.P. acquired funding; M.M., P.Ka. performed the experiments under the guidance of B.P. and J.S.; P.K. synthesized liquid crystal; R.Ma., P.M., and W.P. constructed and fabricated the LC microcavity; D.U., R.M., I.G. fabricated the DBR mirrors and the polymer layer with encapsulation and performed the basic optical characterization; M.F. and U.S. provided the polymer; D.D. performed single-shot coherence measurements; P.K., D.D.S., and G.M. performed theoretical analysis. All authors participated in the interpretation of experimental data; J.S. and G.M. supervised

the project; P.K., M.M., G.M., D.D.S.,J.S. wrote the manuscript with input from all other authors. M.M., P.K., D.D.S. and G.M. proposed the visualization of experimental and theoretical data.

**Competing interests** The authors declare no competing interests.

**Correspondence** Correspondence should be addressed to G. Malpuech ([guillaume.malpuech@uca.fr](mailto:guillaume.malpuech@uca.fr)), J. Szczytko ([jacek.szczytko@fuw.edu.pl](mailto:jacek.szczytko@fuw.edu.pl)).

## **Figure Legends**